Check for updates

Facile synthesis of highly conductive MoS₂/graphene nanohybrids with hetero-structures as excellent microwave absorbers†

Jixing Chai,‡[ab] Deqing Zhang,‡*[ab] Junye Cheng,[cd] Yixuan Jia,[b] Xuewei Ba,[b] Ya Gao,[e] Lei Zhu,[f] Hao Wang*[c] and Maosheng Cao [ID] *[g]

Two-dimensional (2D) MoS₂/graphene nanosheet (MoS₂/GN) hybrids have been demonstrated to be promising microwave absorption (MA) materials due to their unique chemical and physical properties as well as rich impedance matching. However, the reported strategies for preparing MoS₂/GN hybrids have limited their application potential due to the complex, high-cost and inefficient preparation processes. On the other hand, it is of note that the main source of graphene is based on converting insulating graphene oxides (GO) back to conductive reduced graphene oxides (RGO). Thus, the MA performance of obtained MoS₂/RGO nanohybrids is greatly affected by the conversion process of GO. In this work, we prepared the MoS₂/GN hybrids by a facile hydrothermal method with directly introducing highly pure and electroconductive GNs. It is found that the highest reflection loss value of the sample-wax containing 40% MoS₂/GN is −57.31 dB at a thickness of 2.58 mm, and the bandwidth of RL values less than −10 dB can reach up to 12.28 GHz (from 5.72 to 18 GHz) when an appropriate absorber thickness between 1.5 and 4 mm is chosen. The excellent MA performances emanate from effective conjugation of MoS₂ with GN (Mo−C bond between the interfaces), which provides the dielectric loss caused by multi-relaxation, conductance, and polarization. Taking into account the facile synthesis route and their excellent MA performance, the MoS₂/GNs hybrid nanosheets and those composite materials with similar isomorphic hetero-structures are very promising for a wide range of MA applications.

1. Introduction

With more and more electronic communication devices around us, the resulting electromagnetic pollution is becoming a threat to human beings. Therefore, designing and preparing efficient microwave absorbing (MA) materials is crucial to governing electromagnetic pollution.[1–6] Two-dimensional (2D) materials, specially molybdenum disulfide (MoS₂), have attracted attention as MA materials due to their size effect, high specific surface areas and remarkable mechanical properties.[7–11] However, the further application of pure MoS₂ is limited by narrow bandwidth; low RL value and the poor impedance matching of single component materials.[12–15]

Therefore, one of the strategies is introducing a second phase, such as magnetic ferrite (Fe₃O₄),[16,17] carbon materials (CNT, GN),[18,19] and conductive polymers (PEDOT),[20,21] into/onto the matrix to improve the MA performance and enrich impedance matching.[22–24] Zhang *et al.*[25] synthesized MoS₂/Fe₃O₄ hybrids through a hydrothermal and coprecipitation method and they exhibited outstanding MA performance. Pan *et al.*[26] reported a porous coin-like Fe@MoS₂ composite which optimized impedance matching and showed efficient microwave absorption. Zhang *et al.*[27] fabricated MoS₂/PANI-NDs composites *via* an *in situ* oxidation polymerization which exhibited tunable electromagnetic wave attenuation performance. Liu *et al.*[28] prepared 3D hierarchical MoS₂ nanosheets/ultralong N-doped carbon nanotubes as a high-performance electromagnetic wave absorbing material.

Among these second phase materials, graphene shows great potential due to its exclusive structures and electrical properties. Wang *et al.*[29] first synthesized MoS₂/RGO hybrids by

ᵃHeilongjiang Provincial Key Laboratory of Polymeric Composite Materials, Qiqihar University, Qiqihar 161006, China. E-mail: zhdqing@163.com

ᵇSchool of Materials Science and Engineering, Qiqihar University, Qiqihar 161006, China

ᶜGuangdong Provincial Key Laboratory of Micro/Nano Optomechatronics Engineering, College of Mechatronics and Control Engineering, Shenzhen University, Shenzhen 518060, China. E-mail: whao@szu.edu.cn

ᵈCenter of Super-Diamond and Advanced Films, Department of Materials Science and Engineering, City University of HongKong, HongKong 999077, China

ᵉSchool of Chemistry and Chemical Engineering, Qiqihar University, Qiqihar 161006, China

ᶠSchool of Communication and Electronic Engineering, Qiqihar University, Qiqihar 161006, China

ᵍSchool of Materials Science and Engineering, Beijing Institute of Technology, Beijing 100081, China. E-mail: caomaosheng@bit.edu.cn

† Electronic supplementary information (ESI) available. See DOI: 10.1039/c8ra08086k

‡ These authors contributed equally to this work.

chemical vapor deposition and the highest reflection loss value is −50.9 dB. Ran et al.[30] reported the synthesis of MoS_2/RGO hybrids by a three-step ultrasonic method and that the highest reflection loss value was −49.7 dB. It should be noted that the preparation of MoS_2/graphene hybrids with hetero-structures involves the conversion of insulating GO into conductive RGO using reducing agents or high-temperature thermal annealing treatments.[31,32] The conversion process is usually tedious and with some troubles, such as insufficient conductivity recovery, morphological changes, phase transitions, even samples polluted with reducing agents. And the reported preparation of MoS_2/graphene hybrids with pure GNs is inefficient and high-cost, which is not viable from the viewpoint of practical application.

In this work, we develop a hydrothermal method to prepare dielectric MoS_2-nanosheets (MoS_2-NS) and MoS_2/GN hybrids with hetero-structures, using molybdic acid; thiourea to grow on pure GN (Scheme 1). This synthesis strategy for MoS_2 and MoS_2/GN hybrids could be applied in various research areas including catalysis, environmental remediation and hydrogen evolution. The as-synthesized MoS_2/GN hybrids show efficient MA performance, and we also investigate the MA performance mechanisms of MoS_2/GN hybrids.

2. Experimental

All chemicals were in analytical grade and used without further purification. Molybdic acid ($H_2MoO_4 \geq 85\%$) was purchased from Shanghai Aladdin Biochemical Technology Co. Ltd. Thiourea (CH_4N_2S) was purchased from Tianjin Fuchen Chemical Reagent Factory. Natural graphite powders were purchased from Qingdao YUBO graphite Technology Co, LTD. Deionized water was purchased from Qiqihar Tianyuan Water Supply Company.

Graphene was prepared from graphite power by a liquid-phase ultrasound method.[15] MoS_2/GN hybrids were prepared by an improved one-step hydrothermal method. Firstly, 40 mg

graphene-nanosheets (GN) was dispersed in 40 mL of ethanol/deionized water mixture (volume ratio: 1/3). Secondly, 0.4 g H_2MoO_4 and 0.75 g CH_4N_2S were added into the above dispersions. After magnetic stirring for 30 min, the mixture was transferred to a 100 ml Teflon-lined autoclave with a magnetic stirring device. After heated and stirred for 10 hours at 200 °C, the mixtures were subsequently cooled down to room temperature at natural circumstances. Finally MoS_2/GN hybrids were washed with deionized water and ethanol for several times and dried at 60 °C under vacuum oven.

The morphology of samples was characterized by transmission electron microscope (TEM: Japan Hitachi H7650). The crystallization properties were investigated by an X-ray diffractometer (Bruker Company, D8) using the Cu-Kα radiation ($\lambda = 0.15418$ nm). The crystal structure of samples was further observed with high-resolution electron microscopy (HRTEM: Tecnai F30). X-ray photoelectron spectra (XPS) were recorded using a Thermo Scientific ESCALAB MK II with an Mg Kα excitation source. Raman spectroscopy measurements were performed via a Lab RAM HA Evolution. The complex permittivity and permeability were measured in a frequency range of 2–18 GHz with a coaxial wire method using an Agilent N5244A network analyzer.

3. Results and discussion

The XRD patterns of GN; MoS_2 and MoS_2/GN are shown in Fig. S1† and 1a. The MoS_2-nanosheets show diffraction peaks at $2\theta = 14.6°, 32.8°, 39.8°$ and $58.5°$ corresponding to the (002), (100), (103), and (110) planes (PDF37-1492). It is worth noting that there are no diffraction peaks for GN at the patterns of MoS_2/GN hybrids, suggesting the weak scattering power and low crystallinity of very small amount of GNs added. However, the existence of GNs in the hybrid could be identified by Raman spectroscopy (Fig. 1b). There are two strong peaks located at 1345 and 1587 cm^{-1}, which correspond to the D- and G-bands for GNs. It is also observed that the weak E_{2g} and A_{1g} peaks
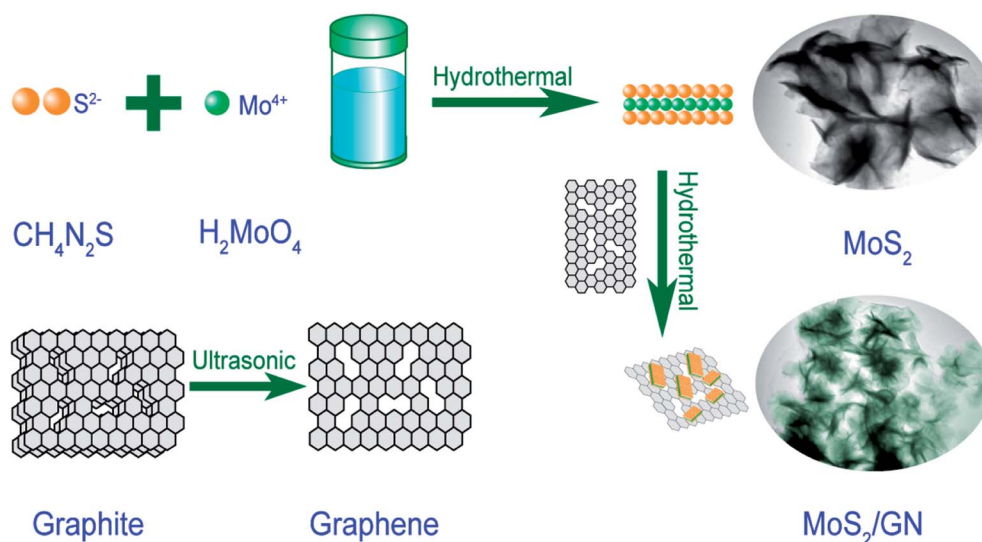
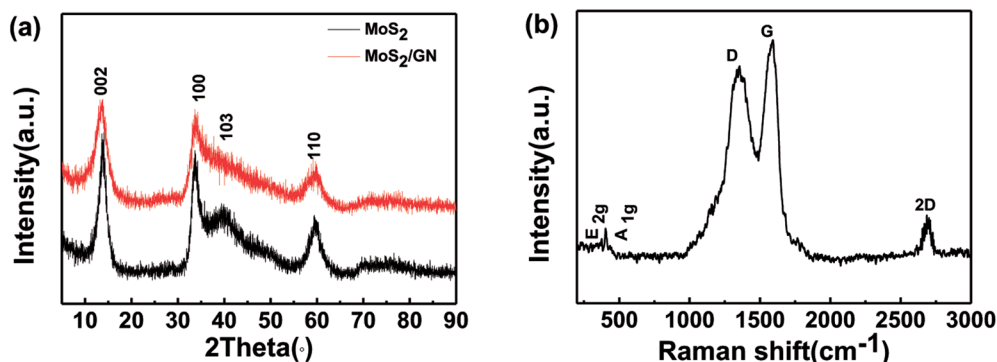Scheme 1 Synthetic route for the MoS_2/GN hybrids.

Fig. 1 (a) X-ray powder diffraction (XRD) patterns for MoS_2 and MoS_2/GN; (b) Raman spectrum for MoS_2/GN.

for MoS_2 are located at 376 and 405 cm^{-1}.[29] In general, the number of layers of graphene is usually determined by the 2D/G ratios. In this work, the 2D/G ratio of MoS_2/GN hybrids is 0.21 (0.07 < 0.21 < 0.3), corresponding to triple-layer graphene sheets,[33] which consistent with pure GN (as shown in Fig. S2†).

Typical morphology information of the MoS_2/GN hybrids is obtained by TEM. Fig. 2a shows that 2D MoS_2 nanosheets look like a flexible flower. The corresponding selected area electron diffraction (SAED) patterns of the MoS_2-nanosheets are also presented in the inset of Fig. 2a, two diffraction rings in the SAED patterns agree well with the (110) and (100) planes of MoS_2. Fig. 2b shows that GN looks thin and light. The overall morphology image of MoS_2/GN hybrids is shown in Fig. 2c. As presented, it can be clearly seen that the flower-like MoS_2-NS are

evenly attached on the GNs. The further micromorphology information of MoS_2/GN composites is displayed by HRTEM, and the interplanar spacing of 0.62 and 0.27 nm observed in Fig. 2d are corresponding to the (002) and (100) planes of hexagonal MoS_2 crystalline structure.[22,34]

The MoS_2/GN hybrids were also characterized by X-ray photoelectron spectroscopy (XPS). As shown in Fig. 3a, there are only the Mo, S, C and O elements in the survey spectrum, and the atomic contents of Mo and S are 15.52% and 31.76%, respectively. The ratio of Mo/S is very close to 1 : 2. The Mo spectrum for MoS_2/GN as shown in Fig. 3b, the bands located at binding energies of 232.05 and 228.75 eV were assigned to the Mo ($3d_{3/2}$) and Mo ($3d_{5/2}$) in the normal state of Mo^{4+} chemical state, respectively. Moreover, the peak deconvolution of the Mo (3d)
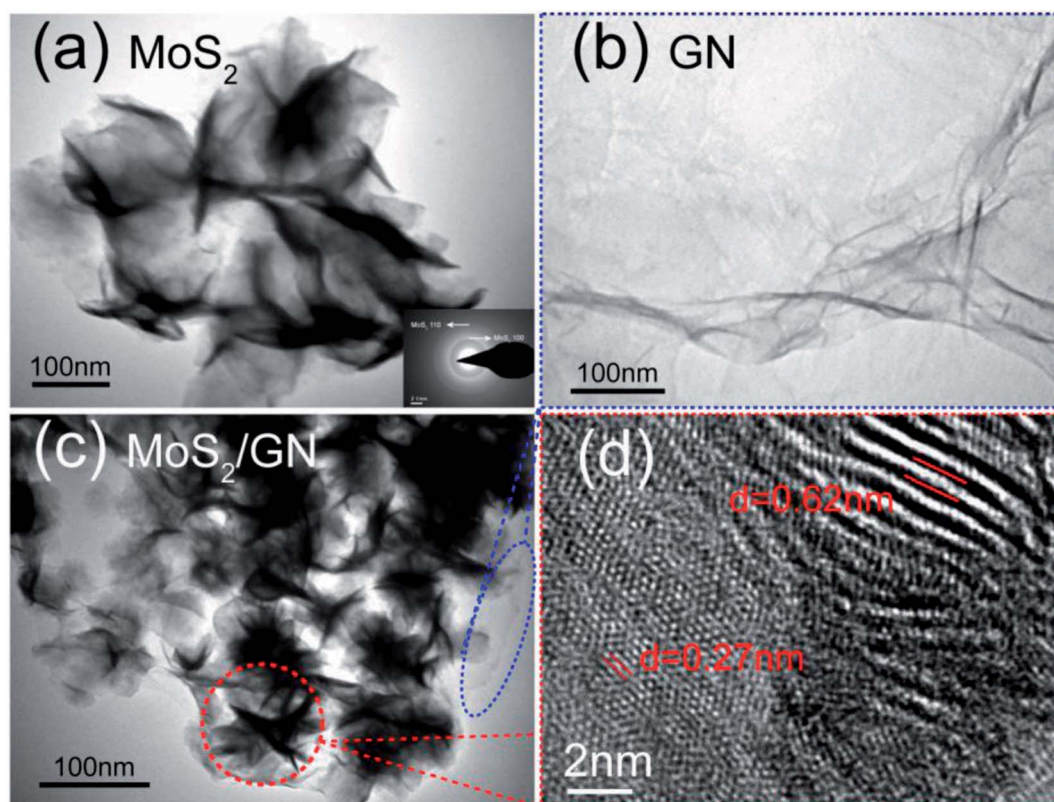

Fig. 2 TEM images of MoS_2 (a); GN (b); MoS_2/GN (c); HRTEM image of MoS_2/GN (d).
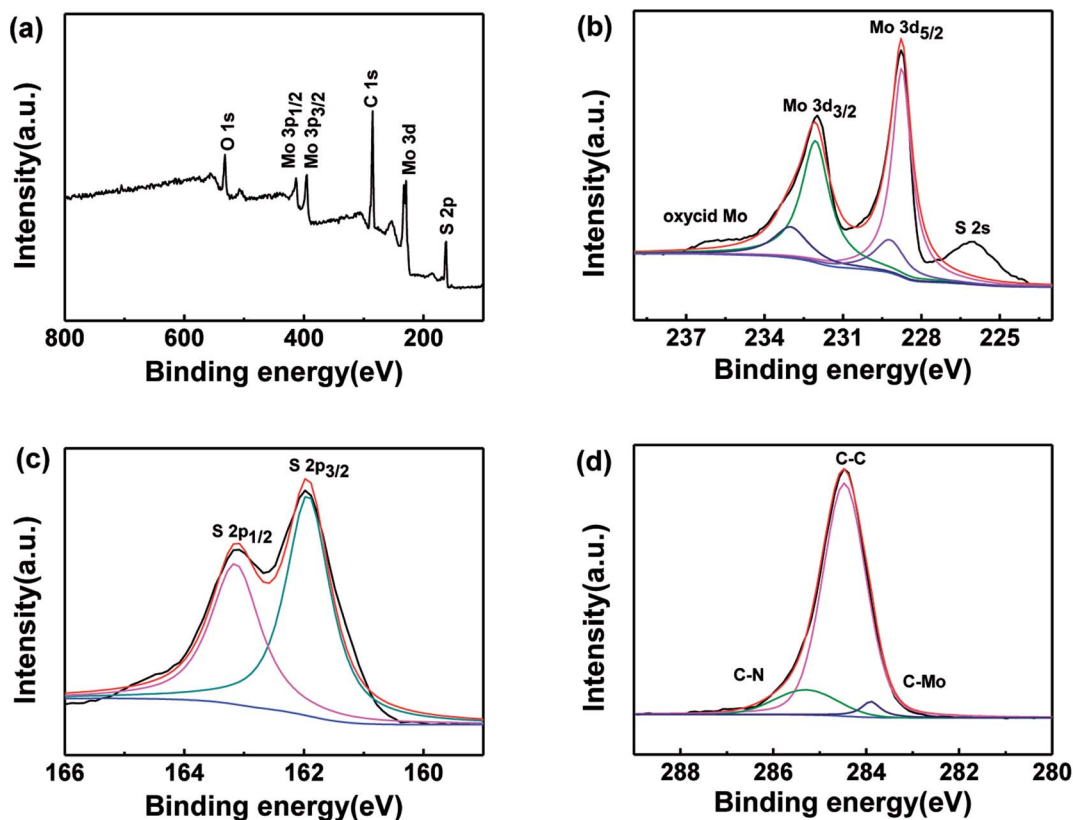
Fig. 3 XPS spectra of the MoS$_2$/GN samples: overall spectrum as marked (a); Mo 3d (b); S 2p (c); C 1s (d).

spectrum of the MoS$_2$/GN hybrids indicated two other weak peaks located at 233.00 and 229.20 eV which were attributed to formation of a Mo–C bond on the hybrids, that is, formation of MoS$_2$/GN hetero-structures. That shows during the prepared process some carbon diffused into the MoS$_2$ to substitute in the lattice of MoS$_2$ at the interfaces.[35–37] The S spectrum of MoS$_2$/GN can be observed to have two peaks located at 162.82 and 161.71 eV, as shown in Fig. 3c, in consistent with the existence of MoS$_2$. The C 1s spectrum can be deconvoluted into two peaks located at 285.30 and 284.47 eV (Fig. 3d), which correspond to the C–N and C–C functionalities, respectively. Moreover, the band located at 283.90 eV was assigned to the presence of the Mo–C bond, which also proved the formation of hetero-structures.

The MA performance can be evaluated by the values of reflection loss (RL) *versus* frequency which can be determined according to transmission line theory.[38–41] The RL is calculated with the following formulas:

$$R_L = 20 \log \frac{|Z_{in} - Z_0|}{|Z_{in} + Z_0|} \tag{1}$$

where the normalized input impedance (Z_{in}) is given by

$$Z_{in} = \sqrt{\frac{\mu_r}{\varepsilon_r}} \tanh \left[j \frac{2\pi}{c} \sqrt{\mu_r \varepsilon_r} fd \right] \tag{2}$$

where Z_0 is the impedance of free space, c is the velocity of light, f is the frequency, and d is the thickness of the absorber. ε_r is the complex permittivity, $\varepsilon = \varepsilon' - j\varepsilon''$, μ_r is the complex permeability, $\mu = \mu' - j\mu''$.

Fig. 4 shows the RL curves of MoS$_2$–wax composites and MoS$_2$/GN–wax composites with different loading contents (from 30 to 50 wt%) in the frequency range of 2–18 GHz at the thickness of 2.5 mm. It can be found that under the same loading of 40 wt%, the value of RL for MoS$_2$/GN hybrid (−43.68 dB) is much larger than that of pure MoS$_2$ (−19.83 dB). For the MoS$_2$/GN-wax composites, it can be found that the MA performance of MoS$_2$/GN-wax composites improves with the increasing loading of MoS$_2$/GN from 30 to 40 wt%. Nevertheless, degraded MA performance is also observed for the sample with the MoS$_2$/GN loading of 50 wt%. In summary, the MoS$_2$/GN–wax
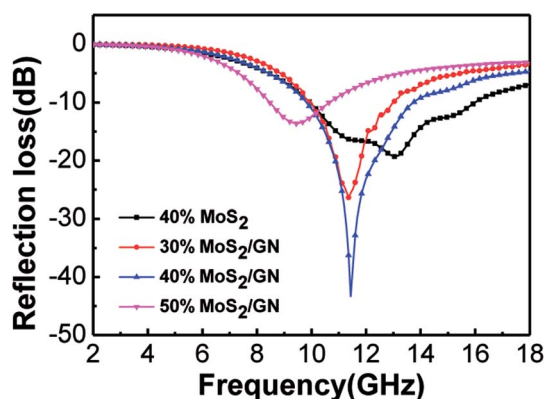

Fig. 4 RL curves of MoS$_2$ and MoS$_2$/GN composites mixed with paraffin with different loading (thickness: 2.5 mm, frequency: 2–18 GHz).

composites containing 40 wt% loading exhibited the outstanding microwave absorption properties.

Fig. 5 shows the RL value and 3D plots for MoS$_2$–wax composites, GN–wax composites and MoS$_2$/GN–wax composites with different thickness (40 wt% loading). The minimum RL is observed to be −57.31 dB at 11.03 GHz for MoS$_2$/GN with a thickness of 2.58 mm; the bandwidth of RL values less than −10 dB can reach up to 12.28 GHz (from 5.72 to 18 GHz) when an appropriate absorber thickness between 1.0 and 4 mm is chosen (as shown Fig. 5a). Compared with the MoS$_2$/GN hybrids, the MoS$_2$-NS and GN-NS exhibit poor MA performances (Fig. 5b and c), indicating that the combination of MoS$_2$ with GN is an effective method in improving the MA performance.

The permittivity and permeability of MoS$_2$ and MoS$_2$/GN with 40 wt% loadings were investigated to better understand the probable mechanism of dielectric loss or magnetic loss. Fig. 6 shows the complex permittivity; complex permeability and dielectric loss tangents (tan $\delta_e = \varepsilon''/\varepsilon'$) of MoS$_2$ and MoS$_2$/GN

hybrid in the range of 2–18 GHz. Obviously, as shown in Fig. 6a, both real (ε') and imaginary (ε'') permittivity of MoS$_2$/GN are found higher than that of pure MoS$_2$, and both real ε' and ε'' decrease with increasing frequency. As shown in Fig. 6b, the values of μ' and μ'' for both MoS$_2$ and MoS$_2$/GN are low, and are close to 1 and 0, respectively. As shown in Fig. 6c, the dielectric loss tangent of MoS$_2$/GN is higher than that of pure MoS$_2$.

In general, the change of complex permittivity can be explained according to Debye theory:[42–45]

$$\varepsilon' = \varepsilon_\infty + \frac{\varepsilon_s - \varepsilon_\infty}{1 + \omega^2 \tau^2} \tag{3}$$

$$\varepsilon'' = \frac{\varepsilon_s - \varepsilon_\infty}{1 + \omega^2 \tau^2} \omega\tau + \frac{\sigma}{\omega \varepsilon_0} \tag{4}$$

where ε_s, ε_∞, ω, τ, σ, and ε_0 are the static permittivity, the relative dielectric permittivity at the high frequency limit, the angular frequency, the polarization relaxation time, the electrical conductivity and the dielectric constant in vacuum, respectively.
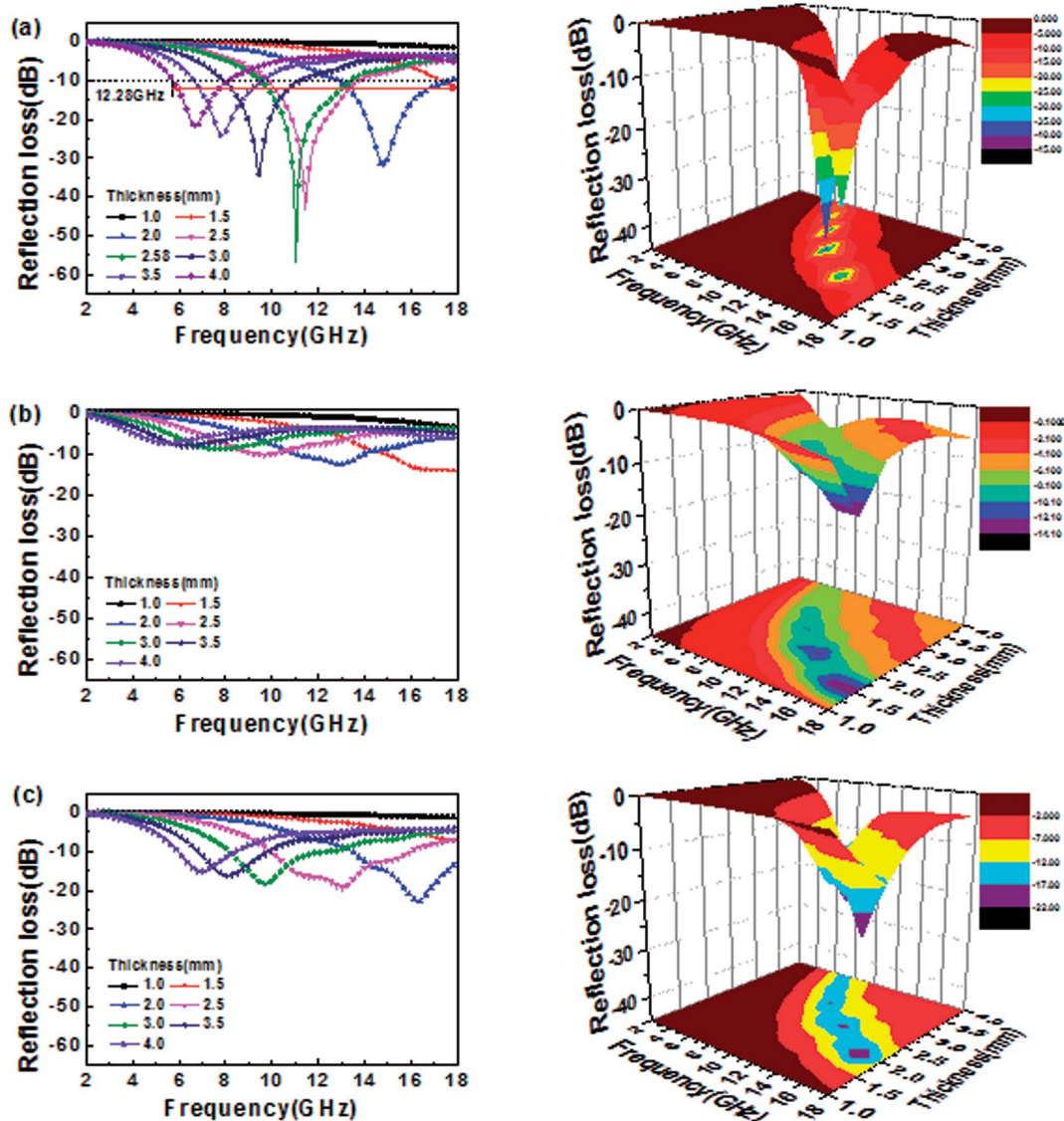

Fig. 5 RL curves and 3D plots for MoS$_2$/GN–wax (a); GN–wax (b); and MoS$_2$–wax (c) composites.
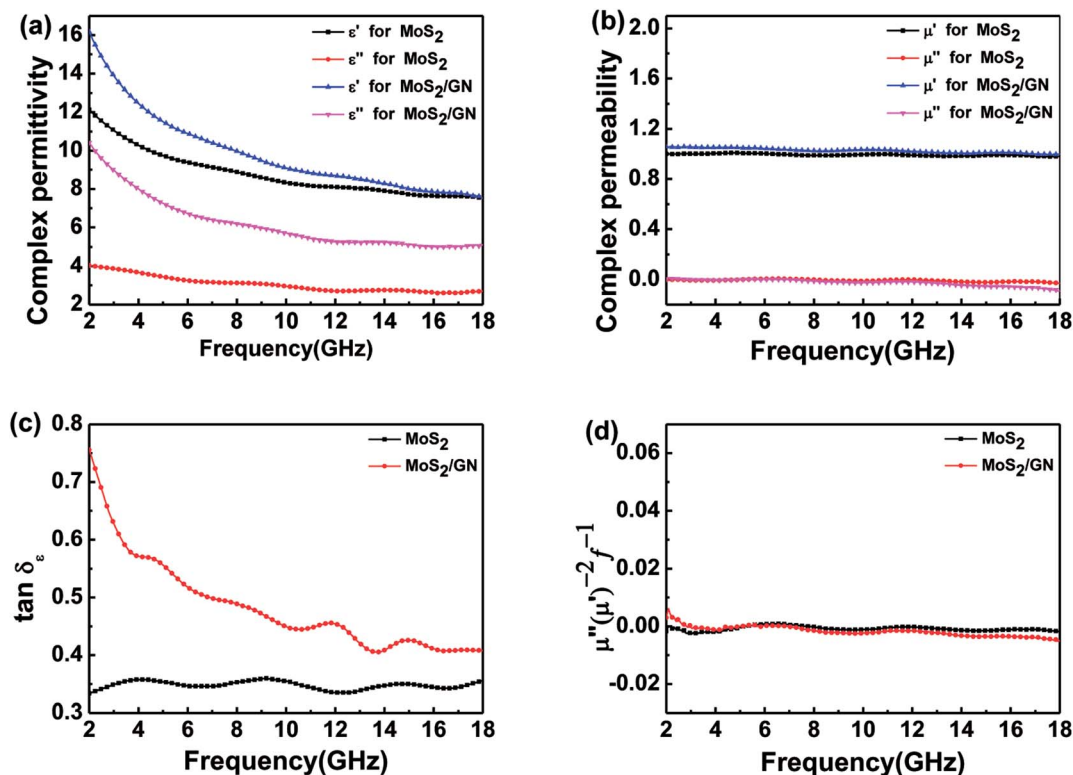
Fig. 6 The complex permittivity (a); and complex permeability (b); the dielectric loss (c) and the values of $C_0 = \mu''(\mu')^{-2}f^{-1}$ (d) in the range of 2–18 GHz for MoS$_2$ and MoS$_2$/GN composites.

According to eqn (3) and (4), the decrease in ε' and ε'' is attributed to the increase in ω. The ε' of MoS$_2$/GN is larger than that of MoS$_2$, which is due to the abundant defect polarization of GNs and interfacial polarization caused by interface coupling of MoS$_2$ and GNs. The electrical conductivities of the samples were measured by four probe conductivity meter. The conductivity of pure GNs and MoS$_2$/GN hybrids (the addition amount of GN is 10 wt%) are 27 800 S m^{-1} and 109.5 S m^{-1}, respectively. Compared to reported MoS$_2$/RGO composites, the conductivity of MoS$_2$/GN hybrids in this work is close to that of 30 wt% RGO addition amount of MoS$_2$/RGO hybrids (113.3 S m^{-1}) in the literature.[13] The highly conductive MoS$_2$/GN hybrids stem from the high electrical conductive GNs. According to the free electron theory,[14] $\varepsilon'' = 1/2\varepsilon_0\pi\rho f$, where ε_0, ρ and f are the permittivity of vacuum, the resistivity and the frequency of the electromagnetic wave, respectively. Therefore, the high electrically conductive GNs result in the enhanced ε'' values of MoS$_2$/GN. The μ' and μ'' for both MoS$_2$ and MoS$_2$/GN are low and no obvious changes appear due to lack of magnetic components in the composite-wax of MoS$_2$ and MoS$_2$/GNs. However, possible magnetic loss for MoS$_2$ and MoS$_2$/GN were also investigated. As shown in Fig. 6d, the value of $\mu''(\mu')^{-2}f^{-1}$ is almost a constant within the range of 4–18 GHz, indicating that the eddy current loss is the main contribution of the magnetic loss in MoS$_2$ and MoS$_2$/GN at 4.0–18.0 GHz.

As presented, the MA performance of MoS$_2$ and MoS$_2$/GN are mainly determined by dielectric loss. In order to investigate and better understand the dielectric loss, the relationship between the relative complex permittivity is expressed by the equation:

$$\left(\varepsilon' - \frac{\varepsilon_s + \varepsilon_\infty}{2}\right)^2 + (\varepsilon'')^2 = \left(\frac{\varepsilon_s + \varepsilon_\infty}{2}\right)^2 \qquad (5)$$

which corresponds to a circle centered at $((\varepsilon_s + \varepsilon_\infty)/2, 0)$ in the spectrum, representing the Debye relaxation process. The Cole–Cole plots further demonstrate the existing of multi-relaxation in MoS$_2$ and MoS$_2$/GN samples, as shown in Fig. 7a and b. Two peaks of ε'' diverge from the ideal Cole–Cole semicircles, indicating the leakage conductance in the MoS$_2$ and MoS$_2$/GN samples. It well illustrates that both relaxation loss and conduction loss play important roles in dielectric loss.

In this work, the excellent MA performance of MoS$_2$/GN hybrid is ascribed to the following factors. First, as shown in Fig. 8a, the addition of GN adjusts the complex permittivity of MoS$_2$ nanosheets, which facilitates impedance matching. Second, the additional GN also carries abundant defects (such as imperfect carbon for GN), providing a large number of dipoles, which are very helpful for dielectric relaxation. Meanwhile, the interfacial polarization in MoS$_2$/GN, which is considered as the capacitor-like structure, could be effective in the adsorption of electromagnetic waves (Fig. 8b). It could be supported by the mechanism of multi-polarization reported by Cao et al.[46] Third, electrons can absorb energy and leap on the composite nanosheets, resulting in eddy current losses (Fig. 8c). It also could be supported by Cao's Electron-Hopping model and Conductive–Network equation.[47] Fourth, the multiple scattering also plays a significant role in electromagnetic wave attenuation as shown in Fig. 8d, the sandwiched layers could
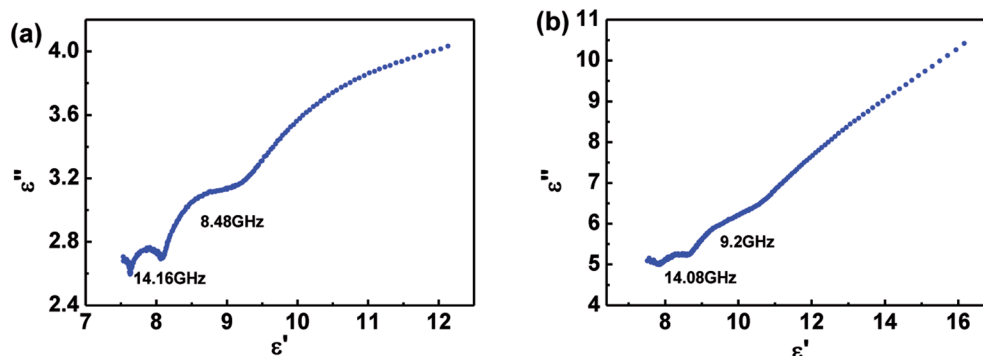
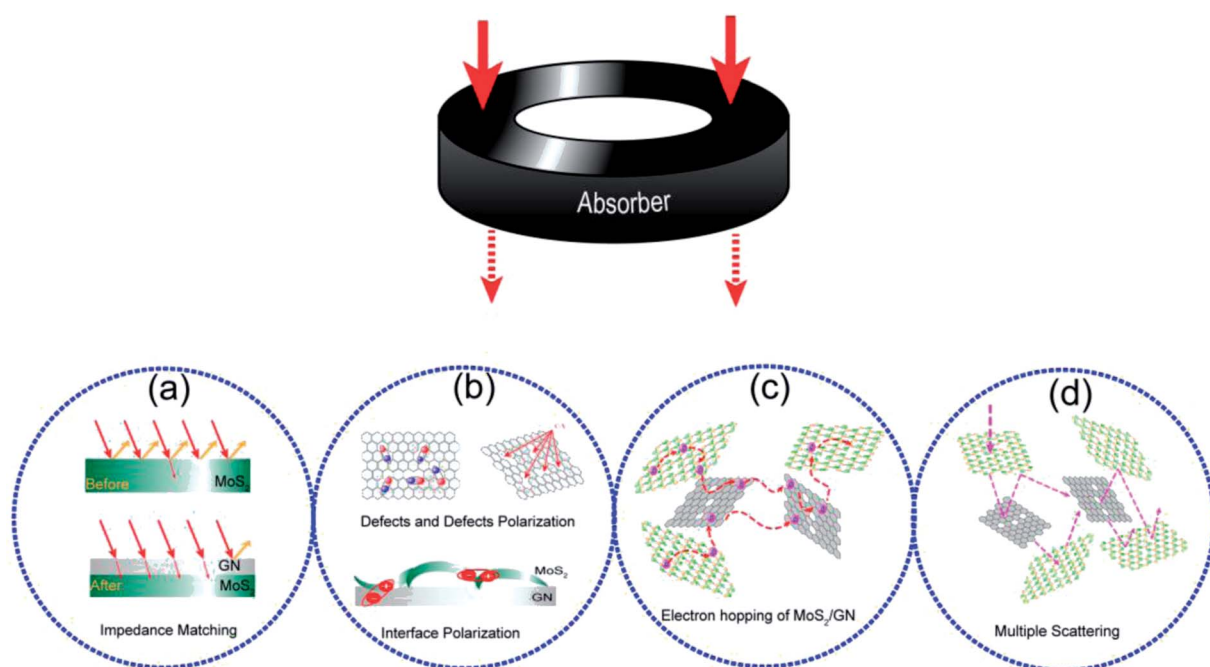Fig. 7 The cole−cole plot of MoS$_2$ (a) and MoS$_2$/GN (b).

Fig. 8 (a) Impedance matching of MoS$_2$/GN; (b) defects and defects polarization of GN; interface polarization of MoS$_2$/GN; (c) electron hopping of MoS$_2$/GN; (d) multiple scattering of MoS$_2$/GN.

Table 1 Electromagnetic wave absorption performance of MA materials

	Method	Thickness (mm)	Minimum RL value (dB)	Loading ratio (wt%)	Effective bandwidth (GHz)	Ref.
MoS$_2$/GN	Liquid phase stripping, hydrothermal	2.58	−57.31	40	12.28	This work
MoS$_2$	Hydrothermal	2.0	−22.85	40	4.5	This work
MoS$_2$	Liquid phase stripping	2.4	−38.42	60	4.16	12
MoS$_2$/RGO	Hummers, chemical vapor deposition	1.9	−50.9	10	5.72	29
MoS$_2$/RGO	Hummers, hydrothermal	2.5	−41.53	10	5.92	13
MoS$_2$/RGO	Hummers, hydrothermal	2.4	−41.9	30	5.8	14
M/MoS$_2$/RGO	Hummers, liquid phase ultrasound	2.5	−49.7	18	5.81	30
MoS$_2$/GN	Liquid phase stripping, hydrothermal	2.2	−55.3	20	5.6	15

lead to the inter-layer reflection and continuous loss of electromagnetic waves. Fifth, the materials with good electrical conductivity may produce skin effect and additional reflection at the surface between materials and air,[48] which offers effective electromagnetic attenuation.

As listed in Table 1, compared with the previously reported MoS$_2$/graphene MA materials, the minimum RL value of MoS$_2$/GN hybrids in this work is higher than those of MoS$_2$/RGO hybrids in previous reports. Meanwhile, it is also shown that the minimum RL value of MoS$_2$/RGO prepared by chemical vapor

deposition is higher than that of MoS$_2$/RGO prepared by hydrothermal method. This is because the chemical vapor deposition can help convert more insulating GO back to conductive RGO.

4. Conclusion

In summary, MoS$_2$ and MoS$_2$/GN hybrids were prepared by a facile one-step hydrothermal method, and the MoS$_2$-nanosheets were conjugated on the highly conductive GNs. The mechanisms of MA performance for MoS$_2$ and MoS$_2$/GN were also investigated. The excellent MA performance indicates that the MoS$_2$/GN hybrids with hetero-structures hold some advantages in both high conductance and high absorption performance devices. It is also believed that the simple hydrothermal method can promote the synthesis of hetero-structures nanohybrids at an industrial scale. Furthermore, the hetero-structure nanohybrids could also be readily applied in other fields.

Conflicts of interest

There is no conflict in the statement.

Acknowledgements

References

1 W. L. Song, M. S. Cao, L. Z. Fan, M. M. Lu, Y. Li, C. Y. Wang and H. F. Ju, *Carbon*, 2014, **77**, 130–142.

2 L. L. Yan, X. X. Wang, S. C. Zhao, Y. Q. Li, Z. Gao, B. Zhang, M. S. Cao and Y. Qin, *ACS Appl. Mater. Interfaces*, 2017, **9**, 11116–11125.

3 W. L. Song, X. T. Guan, L. Z. Fan, W. Q. Cao, C. Y. Wang, Q. L. Zhao and M. S. Cao, *J. Mater. Chem. A*, 2017, **3**, 2097–2107.

4 B. Zhao, C. X. Zhao, M. Hamidinejad, C. D. Wang, R. S. Li, S. Wang, Y. Kazemi and C. B. Park, *J. Mater. Chem. C*, 2018, **6**, 10292–10300.

5 W. L. Song, X. T. Guan, L. Z. Fan, Y. B. Zhao, W. Q. Cao, C. Y. Wang and M. S. Cao, *Carbon*, 2016, **100**, 109–117.

6 S. Motojima, S. Hoshiya and Y. Hishikawa, *Carbon*, 2003, **41**, 2658–2660.

7 X. Liu, L. S. Wang, Y. T. Ma, H. F. Zheng, L. Lin, Q. F. Zhang, Y. Z. Chen, Y. L. Qiu and D. L. Peng, *ACS Appl. Mater. Interfaces*, 2017, **9**, 7601–7610.

8 X. Sun, J. P. He, G. X. Li, J. Tang, T. Wang, Y. X. Guo and H. R. Xue, *J. Mater. Chem. C*, 2012, **1**, 765–777.

9 M. S. Cao, J. Zhu, J. Yuan, T. F. Zhang, Z. H. Peng, Z. J. Guo, G. Xiao and S. M. Qin, *Mater. Des.*, 2002, **23**, 557–564.

10 M. Q. Zeng, Y. Xiao, J. X. Liu, K. N. Yang and L. Fu, *Chem. Rev.*, 2018, **118**, 6236–6296.

11 B. Zhao, L. Y. Liang, J. S. i. Deng, Z. Y. Bai, J. W. Liu, X. Q. Guo, K. Gao, W. H. Guo and R. Zhang, *CrystEngComm*, 2017, **19**, 6579–6587.

12 M. Q. Ning, M. M. Lu, J. B. Li, Z. Chen, Y. K. Dou, C. Z. Wang, F. Rehman, M. S. Cao and H. B. Jin, *Nanoscale*, 2015, **7**, 15734–15740.

13 X. Ding, Y. Huang, S. Li, N. Zhang and J. G. Wang, *Composites, Part A*, 2016, **9**, 424–432.

14 X. X. Wang, W. L. Zhang, X. Q. Ji, B. Q. Zhang, M. X. Yu, W. Zhang and J. Q. Liu, *RSC Adv.*, 2016, **6**, 106187–106193.

15 D. Q. Zhang, Y. X. Jia, J. Y. Cheng, S. M. Chen, J. X. Chai, X. Y. Yang, Z. Y. Wu, H. Wang, W. J. Zhang, Z. L. Zhao, C. Han, M. S. Cao and G. P. Zheng, *J. Alloys Compd.*, 2018, **758**, 62–71.

16 X. H. Li, H. B. Yi, J. W. Zhang, J. Feng, F. S. Li, D. S. Xue, H. L. Zhang, Y. Peng and N. J. Mellors, *J. Nanopart. Res.*, 2013, **15**, 1472.

17 G. B. Sun, B. X. Dong, M. H. Cao, B. Q. Wei and C. W. Hu, *Chem. Mater.*, 2011, **23**, 1587–1593.

18 S. Motojima, Y. Noda, S. Hoshiya and Y. Hishikawa, *J. Appl. Phys.*, 2003, **94**, 2325–2330.

19 M. Q. Ning, J. B. Li, B. Y. Kuang, C. Z. Wang, D. Z. Su, Y. J. Zhao, H. B. Jin and M. S. Cao, *Appl. Surf. Sci.*, 2018, **447**, 244–253.

20 P. B. Liu, Y. Huang and X. Zhang, *Powder Technol.*, 2015, **276**, 112–117.

21 W. C. Zhou, X. J. Hu, C. H. Sun, J. Yan, S. Y. Zhou and P. Chen, *Polym. Adv. Technol.*, 2014, **25**, 83–88.

22 M. S. Cao, J. Yang, W. L. Song, D. Q. Zhang, B. Wen, H. B. Jin, Z. L. Hou and J. Yuan, *ACS Appl. Mater. Interfaces*, 2012, **4**, 6949–6956.

23 W. Feng, Y. M. Wang, J. C. Chen, L. X. Guo, J. H. OuYang, D. C. Jia and Y. Zhou, *Phys. Chem. Chem. Phys.*, 2017, **19**, 14596–14605.

24 G. S. Wang, Y. Wu, Y. Z. Wei, X. J. Zhang, Y. Li, L. D. Li, B. Wen and M. S. Cao, *Chempluschem*, 2014, **79**, 375–381.

25 D. Q. Zhang, J. X. Chai, J. Y. Chen, Y. X. Jia, X. Y. Yang, H. Wang, Z. L. Zhao, C. Han, G. C. Shan, W. J. Zhang, G. P. Zheng and M. S. Cao, *Appl. Surf. Sci.*, 2018, **462**, 872–882.

26 J. J. Pan, X. Sun, T. Wang, Z. T. Zhu, Y. P. He, W. Xia and J. P. He, *Appl. Surf. Sci.*, 2018, **457**, 271–279.

27 W. L. Zhang, D. G. Jiang, X. X. Wang, B. N. Hao, Y. D. Liu and J. Q. Liu, *J. Phys. Chem. C*, 2017, **121**, 4989–4998.

28 L. L. Liu, S. Zhang, F. Yan, C. Y. Li, C. L. Zhu, X. T. Zhang and Y. J. Chen, *ACS Appl. Mater. Interfaces*, 2018, **10**, 14108–14115.

29 Y. F. Wang, D. L. Chen, X. Yin, P. Xu, F. Wu and M. He, *ACS Appl. Mater. Interfaces*, 2015, **7**, 26226–26234.

30 J. Ran, L. X. Shen, L. Zhong and H. Q. Fu, *Ind. Eng. Chem. Res.*, 2017, **56**, 10667–10677.

31 W. L. Song, X. T. Guan, L. Z. Fan, W. Q. Cao, C. Y. Wang and M. S. Cao, *Carbon*, 2015, **93**, 151–160.

32 X. Liang, B. Quan, G. B. Ji, W. Liu, H. W. Zaho, S. S. Dai, J. Lv and Y. W. Du, *ACS Sustainable Chem. Eng.*, 2017, **5**, 10570–10579.

33 O. Akhavan, *Carbon*, 2018, **81**, 158–166.

34 Y. Shi, Y. Zhou, D. R. Yang, W. X. Xu, C. Wang, F. B. Wang, J. J. Xu, X. H. Xia and H. Y. Chen, *J. Am. Chem. Soc.*, 2017, **139**, 15479–15485.

35 O. Akhavan, *Appl. Surf. Sci.*, 2010, **257**, 1724–1728.

36 O. Akhavan and E. Ghaderi, *J. Phys. Chem. C*, 2009, **113**, 20214–20220.

37 X. W. Zhang and L. C. Lei, *Appl. Surf. Sci.*, 2008, **254**, 2406–2412.

38 X. B. Li, S. W. Yang, J. Sun, P. He, X. P. Pu and G. Q. Ding, *Synth. Met.*, 2014, **194**, 52–58.

39 Y. H. Chen, Z. H. Huang, M. M. Lu, W. Q. Cao, J. Yuan, D. Q. Zhang and M. S. Cao, *J. Mater. Chem. A*, 2015, **3**, 12621–12625.

40 B. Zhao, J. W. Liu, X. Q. Guo, W. Y. Zhao, L. Y. Liang, C. Ma and R. Zhang, *Phys. Chem. Chem. Phys.*, 2017, **19**, 9128–9136.

41 B. Zhao, X. Q. Guo, Y. Y. Zhou, T. T. Su, C. Ma and R. Zhang, *CrystEngComm*, 2017, **19**, 2178–2186.

42 C. L. Zhu, M. L. Zhang, Y. J. Qiao, G. Xiao, F. Zhang and Y. J. Chen, *J. Phys. Chem. C*, 2010, **114**, 16229–16235.

43 B. Zhao, X. Q. Guo, W. Y. Zhao, J. S. Deng, B. B. Fan, G. Shao, Z. Y. Bai and R. Zhang, *Nano Res.*, 2017, **1**, 331–343.

44 B. Zhao, X. Q. Guo, W. Y. Zhao, J. S. Deng, G. Shao, B. B. Fan, Z. Y. Bai and R. Zhang, *ACS Appl. Mater. Interfaces*, 2016, **8**, 28917–28925.

45 B. Zhao, W. Y. Zhao, G. Shao, B. B. Fan and R. Zhang, *ACS Appl. Mater. Interfaces*, 2015, 7, 12951–12960.

46 W. L. Song, X. T. Guan, L. Z. Fan, W. Q. Cao, Q. L. Zhao, C. Y. Wang and M. S. Cao, *Mater. Res. Bull.*, 2015, **72**, 316–323.

47 Y. L. Zhang, X. X. Wang and M. S. Cao, *Nano Res.*, 2017, **11**, 1426–1436.

48 X. X. Wang, T. Ma, J. C. Shu and M. S. Cao, *Chem. Eng. J.*, 2018, **332**, 321–330.